European Journal of Pharmaceutical Sciences 225 (2026) 107624

Contents lists available at ScienceDirect

European Journal of Pharmaceutical Sciences

journal homepage: www.elsevier.com/locate/ejps

Combined second harmonic and linear light scattering as a tool for solubility and aggregation screening

Jitka Kalasová [a,b], Orly Tarun [c], Martin Kuentz [b,*]

[a] University of Basel, Department of Pharmaceutical Sciences, Klingelbergstrasse 50, 4052 Basel, Switzerland
[b] University of Applied Sciences and Arts Northwestern Switzerland, School of Life Sciences, Institute for Pharma Technology and Biotechnology, Hofackerstrasse 30, 4132 Muttenz, Switzerland
[c] ORYL Photonics SA, 1066, Route de la Corniche 5B, Epalinges, Switzerland

ARTICLE INFO

Keywords:
Second harmonic scattering
Linear light scattering
High-throughput screening
Ultrafast laser
Liquid-liquid phase separation
Amorphous drug

ABSTRACT

Poor aqueous solubility and complex supersaturation behaviour of small-molecule drugs require rapid, material-sparing analytical tools that capture incipient aggregation and phase separation events under non-equilibrium conditions. This work evaluated a miniaturised optical platform that combined second harmonic scattering (SHS) with linear light scattering (LLS) driven by an ultrafast 1030 nm laser to monitor supersaturated solutions of 12 poorly water-soluble drugs prepared by DMSO solvent shift in 384-well plates. LLS and SHS signals were recorded after 1 h and 24 h and compared with apparent solubilities from a parallel solvent-shift HPLC assay. LLS, which reports on particle size/number, detected precipitation onsets typically close to or below HPLC values and could resolve particle formation down to ~ 0.1 μM for pimozide, substantially exceeding the sensitivity of standard nephelometric methods. SHS, which is sensitive to interfacial asymmetry and nonlinear susceptibility, often showed onsets and complex peak-drop-rise patterns that deviated from LLS, particularly for lopinavir, loratadine, and ritonavir, indicating structurally distinct, largely centrosymmetric drug-rich assemblies above the solubility limit. Orthogonal characterization by scanning electron microscopy, Capflex (capillary flow with a hydrophobic fluorescent tracer), and confocal fluorescence microscopy provided independent evidence for droplet-like or amorphous drug-rich domains that preceded bulk precipitation. Together, the results showed that combined SHS-LLS enabled highly sensitive detection of precipitation, while revealing multistep, non-classical aggregation pathways in pharmaceutical supersaturated systems.

1. Introduction

The limited aqueous solubility of small-molecule drugs remains a major challenge in pharmaceutical research. Poor solubility can hinder dissolution, absorption, and ultimately oral bioavailability, while complicating the drug candidate progression across discovery, development and formulation phase (Williams et al., 2013). In discovery screening, poor drug solubility can lead to underestimated activity, variable biological assay readouts, and unreliable structure-activity relationships (Di and Kerns, 2006). At later stages, solubility becomes an important factor in formulation strategy, dose feasibility, and reliability of *in vitro* and *in vivo* performance (Bhalani et al., 2022; Di et al., 2012; Williams et al., 2013).

Experimental solubility assessment involves trade-offs among speed, material consumption, and data quality. Classical equilibrium (thermodynamic) assays, particularly shake-flask experiments with high-performance liquid chromatography (HPLC) or ultra-performance liquid chromatography (UPLC) quantification, remain the reference method for accurate solubility measurement, but are relatively slow, labour-intensive, and sample-consuming, even in miniaturised or partially automated formats (Hoelke et al., 2009; Zhou et al., 2007).At the drug discovery stage, the value of thermodynamic assays that require excess amounts of a scarce drug is questionable, particularly when compound purity is still limited and not yet representative of later kilo-lab campaigns. In contrast, high-throughput microplate-based workflows provide rapid, low material readouts but typically measure kinetic solubility, because compounds are mostly introduced from DMSO stocks into aqueous media and precipitation is monitored under non-equilibrium conditions (Alsenz and Kansy, 2007). Kinetic solubility values often exceed thermodynamic solubility and can be strongly

* Corresponding author.
E-mail address: martin.kuentz@fhnw.ch (M. Kuentz).

https://doi.org/10.1016/j.ejps.2026.107624
Received 28 May 2026; Received in revised form 7 July 2026; Accepted 27 July 2026
Available online 28 July 2026

influenced by supersaturation, amorphous versus crystalline solid form, salt formation, cosolvent level (e.g., DMSO), incubation time and assay pH (Alsenz and Kansy, 2007; Saal and Petereit, 2012).

Nonetheless, kinetic solubility and supersaturation measurements remain highly relevant not only in early discovery but also in formulation development, particularly for systems designed to generate non-equilibrium supersaturation rather than reflect equilibrium solubility (Taylor and Zhang, 2016). Many enabling formulations, such as amorphous solid dispersions (ASDs), lipid-based systems, and nanosuspensions, intentionally create transient supersaturation that can lead to liquid-liquid phase separation (LLPS), amorphous or glassy phases, and eventual crystallization (Ilevbare and Taylor, 2013; Ueda et al., 2026). In these systems, the onset and kinetics of aggregation, phase separation, and particle growth are of similar importance to know as the equilibrium solubility, since drug-rich intermediate phases can act as reservoirs that sustain the concentration of molecularly dissolved drug available for absorption (Nora et al., 2022; Ueda et al., 2026). This highlights the need for rapid, material-sparing analytical techniques capable of capturing early colloidal and particulate events, including optical and light-scattering methods that enable real-time monitoring of supersaturation, LLPS, and precipitation.

Building on our recent demonstration that non-resonant second harmonic scattering (SHS) can support high-throughput assessment of aqueous drug solubility and aggregation-related transitions (Kalasová et al., 2025), the present work evaluates an upgraded optical platform that combines SHS with linear light scattering (LLS) using an ultrafast pulsed laser. Using a set of poorly water-soluble drugs, we compare the concentration-dependent responses obtained from both channels and assess where the two signals agree or disagree regarding the onset of aggregation and precipitation. The aim was to examine whether the combined readout offers a sensitive, material-efficient route for solubility assessment while providing additional qualitative insight into concentration-dependent aggregation behaviour, including possible signatures consistent with spherical precipitation or liquid-liquid/liquid-glass phase separation.

2. Materials and methods

2.1. Chemicals

The chemicals used in this study were obtained from different sources. Tolfenamic acid was purchased from AK Scientific (Union City, CA, USA). Lopinavir, carvedilol, bifonazole, pimozide, loratadine, carbamazepine, griseofulvin, albendazole, and ritonavir were obtained from Biosynth (Carbosynth Ltd., Compton, UK). Haloperidol and dipyridamole were purchased from Sigma-Aldrich (Merck KGaA, Taufkirchen, Germany). Anhydrous dimethyl sulfoxide (DMSO), sodium chloride (NaCl), ammonium acetate, and 1-methyl-2-pyrrolidinone (NMP) were purchased from Sigma-Aldrich (Merck KGaA, Taufkirchen, Germany) and used as received.

Phosphate-buffered saline was prepared using Na_2HPO_4 and KH_2PO_4, both purchased from AK Scientific (Union City, CA, USA), and NaCl from Sigma-Aldrich (Merck KGaA, Taufkirchen, Germany), using ultrapure water (conductivity $\leq$ 0.055 µS/cm). Before use, the buffer was filtered through a 0.22 µm syringe filter (Millex®-GS, MCE membrane, Millipore, Burlington, MA, USA).

BODIPY 493/503 was purchased from Thermo Fisher Scientific (Eugene, OR, USA) and used as received.

2.2. SHS-LLS solvent-shift precipitation assay

The precipitation and aggregation behaviour of 12 model drugs was investigated using an ORYL F1 instrument (Oryl Photonics SA, Epalinges, Switzerland). The drugs were measured in phosphate-buffered saline (PBS, 18 mM phosphate, 137 mM NaCl, pH 7.4), prepared according to the European Pharmacopoeia (7.0, 4005000), at ambient temperature. Samples were prepared using a solvent-shift method. A master stock solution of each drug was first prepared in DMSO and subsequently serially diluted (dilution factors varied between compounds) to obtain at least 12 intermediate stock solutions spanning concentrations below and above the expected solubility range. Aliquots of 1 µL of each intermediate stock solution were dispensed into wells of a 384-well plate (cyclic olefin copolymer, Greiner Bio-One GmbH, Frickenhausen, Germany) prefilled with 99 µL of PBS, resulting in a final DMSO content of 1% (v/v). A corresponding blank (1% v/v dimethyl sulfoxide (DMSO) in PBS) was included. All samples were prepared in three independent replicates. The plates were sealed with Titer Tops® sealing film (USA Scientific, Inc., Ocala, FL, USA) to prevent evaporation and contamination of the samples. Following preparation, the plates were centrifuged (Centrifuge 5810 R, Eppendorf, Hamburg, Germany) at 1000 rpm for 1 min to ensure uniform sample distribution and to remove microbubbles. Measurements were performed after 1 h and 24 h of incubation time. Between measurements, the plates were sealed, maintained at room temperature and agitated at 800 rpm using a microplate shaker (Thermo Fisher Scientific, Eugene, OR, USA).

The SHS-LLS assay requires only small amounts of compound. For a 12-point concentration series measured in triplicate, the theoretical in-well consumption was typically in the low-microgram to sub-milligram range, approximately 15 to 500 µg per compound. In practice, low milligram quantities (1 to 3 mg) may still be required for accurate weighing, stock preparation, serial dilution, and unavoidable handling losses.

2.3. SHS-LLS instrumentation and data analysis

Figure 1 illustrates a simplified schematic of the ORYL F1 instrument (Oryl Photonics SA, Epalinges, Switzerland) with combined second harmonic scattering (SHS) and linear light scattering (LLS) channels. An ultrafast laser (1030 nm, repetition rate of 200 kHz, pulse duration of ~ 250 fs; model FS10, NKT Photonics A/S, Birkerød, Denmark) was used as the excitation source. The laser beam was directed onto the liquid sample contained in a microplate (sample volume 100 µL per well) via beam-shaping optics and mirrors.

The transmitted fundamental beam (1030 nm) was blocked using a custom-made beam blocker equipped with a light trap. The scattered

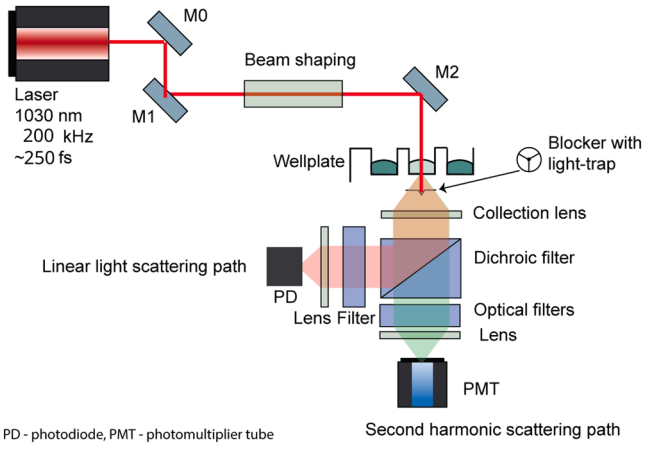

Figure 1. Optical schematic of the ORYL F1 instrument with combined second harmonic and linear light scattering (SHS-LLS) channels. An ultrafast laser is directed onto a liquid sample contained in a microplate. The transmitted fundamental beam is blocked by a beam blocker positioned beneath the microplate. Scattered light is collected by a collection lens and spectrally separated using a dichroic optical element. The linear light scattering (LLS) signal at 1030 nm is filtered and directed to a silicon photodiode (PD), while the second harmonic scattering (SHS) signal at 515 nm is filtered and directed to a photomultiplier tube (PMT).

light generated by the interaction of the excitation beam with the sample was collected using a collection lens and spectrally separated using a dichroic optical element into two detection pathways. The linear light scattering (LLS) signal at 1030 nm was filtered and focused onto a silicon photodiode (PD), while the second harmonic scattering (SHS) signal at 515 nm was passed through a sequence of optical filters and detected using a photomultiplier tube (PMT). The detector outputs from both channels were integrated over a defined number of laser pulses and converted into voltage signals. The acquisition time was set to 50 ms, and each data point was recorded as the mean of 30 consecutive measurements. For each well, a background signal was first recorded with the laser off and automatically subtracted from subsequent measurements, ensuring background-corrected intensities.

Data processing and visualization were performed using RStudio (version 2026.04.0, Posit PBC, Boston, USA). The general workflow for SHS and LLS data analysis, including outlier handling and signal interpretation, followed our previously reported methodology (Kalasová et al., 2025).

Briefly, datasets were inspected for outliers arising from experimental artefacts (e.g., dust particles, fibres, or well plate defects), which can strongly affect scattering signals. Blank samples were cleaned using the interquartile range (IQR) method, and the remaining values (n = 287) were averaged to obtain a representative global blank signal. SHS and LLS datasets were processed and evaluated independently throughout the analysis.

In the present study, the baseline determination was refined to improve robustness. Instead of relying on a fixed set of initial points, the drug-specific baseline was calculated from low-concentration data combined across the replicates. Specifically, the baseline dataset consisted of (i) a globally averaged blank signal and (ii) the k lowest concentration points per replicate (k = 2 to 5, typically 3). These values were pooled to calculate the baseline mean and standard deviation for each drug separately, and an upper threshold was defined as baseline + 3σ (standard deviation). To determine the scattering onset concentration, the concentration-intensity profiles were linearly interpolated over a dense concentration grid for each replicate set. The onset concentration was defined as the first intersection between the interpolated signal curve and the upper threshold. The same analysis workflow was consistently applied to both the SHS and LLS datasets to enable a direct comparison between the nonlinear and linear scattering responses.

2.4. Reference solvent-shift solubility assay followed by HPLC quantification

The apparent solubility of the investigated compounds was determined using a solvent-shift protocol, followed by HPLC quantification. Stock solutions of each compound were prepared in DMSO, typically at 10 to 100 mM. Aliquots of 2 µL were dispensed into wells of 96-well filter plates equipped with 0.22 µm hydrophilic low-protein-binding Durapore® membranes (MultiScreen® GV, Millipore, Burlington, MA, USA) prefilled with 198 µL PBS (pH 7.4), resulting in a final DMSO content of 1% (v/v). The plates were sealed and incubated at room temperature under agitation for either 1 h or 24 h. Separate plates were prepared for each incubation time. After incubation, the plates were centrifuged to separate the undissolved material from the filtrate. The filtrates were diluted 1:1 (v/v) with NMP to prevent precipitation during the analysis.

Chromatographic analysis was performed using an Agilent 1260 Infinity II HPLC system equipped with a 4.6 × 150 mm Eclipse XDB-C18 column (5 µm; Agilent Technologies, Santa Clara, CA, USA). The mobile phase consisted of 10 mM ammonium acetate in water (mobile phase A) and acetonitrile (mobile phase B). Gradient elution was performed at 1.0 mL/min as follows: 90% A at 0 min, 50% A at 1 min, 5% A at 8 min, followed by re-equilibration to 90% A at 9 min. UV detection was performed at compound-specific wavelengths of 221, 245, or 290 nm.

All measurements and calibration curves were performed in triplicate. Data acquisition and analysis were carried out using OpenLAB CDS ChemStation software (version 2.3.54, Agilent Technologies, Santa Clara, CA, USA). The resulting HPLC values are reported as apparent solubilities defined by the applied solvent-shift, 0.22 µm filtration, and chromatographic quantification workflow. The HPLC assay was deliberately designed using a solvent-shift protocol to enable direct comparison with the SHS-LLS assay.

2.5. Scanning electron microscopy (SEM)

The morphology of the precipitated drug particles was examined by scanning electron microscopy (SEM). Samples were prepared at the highest concentration measured in the SHS-LLS experiments. Drug suspensions were prepared using the same solvent-shift procedure as for the SHS-LLS precipitation assay, including identical DMSO drug stock preparation, except that water was used as the aqueous medium instead of PBS. The final DMSO content was 1% (v/v) in all samples. After preparation, 1 to 2 drops of each suspension were deposited onto silicon wafer substrates and dried at 40 °C for 30 min to remove the solvent. The dried samples were sputter-coated with a ~ 4 nm gold layer using an automatic sputter coater (Auto Sputter Coater 108A, Cressington Scientific Instruments, Watford, UK). SEM imaging was performed using a field-emission scanning electron microscope (JSM-IT800, JEOL Ltd., Tokyo, Japan) at an accelerating voltage of 3 kV and a working distance of approximately 9.5 mm.

2.6. Capillary flow experiments (Capflex)

Capillary flow experiments were performed using a FIDA 1 instrument (FIDA Biosystems ApS, Søborg, Denmark) operated in Capflex mode to probe the formation of drug-rich domains under supersaturated conditions. The method is based on flow-induced Taylor dispersion analysis and is described in detail elsewhere (Stender et al., 2021).

BODIPY 493/503 was included as a fluorescent tracer, expected to preferentially partition into nonpolar drug-rich domains. A 2 µM BODIPY solution in DMSO was first prepared and subsequently used as the solvent for drug stock preparation and all dilutions to ensure a constant tracer concentration throughout. Drug stock solutions (10 mM) were prepared in this BODIPY-containing DMSO and diluted accordingly. Aliquots were then introduced into PBS (pH 7.4) and the final samples contained 1% (v/v) DMSO and 20 nM BODIPY.

Measurements of haloperidol (HLP), lopinavir (LPV), loratadine (LRT), and ritonavir (RTV) were performed in standard Capflex mode using an autosampler with continuous sample injection into a fused-silica capillary (1 m length, 75 µm inner diameter). A fluorescence detector with excitation at 485 nm and emission collected through a 510 nm long-pass filter was used. The capillary was filled with buffer prior to sample introduction. Fluorescence signals were recorded as a function of time, where transient intensity spikes correspond to the passage of dye-enriched domains through the detection volume. Experimental parameters for capillary conditioning and sample injection are summarised in Table S1 (Supplementary material).

Fluorescence-time data were processed in RStudio (version 2026.04.0, Posit PBC, Boston, USA). Traces were smoothed using a rolling median filter (window size = 50) to reduce transient artefacts and subsequently fitted with a four-parameter logistic model to describe the baseline signal ($R^2 > 0.99$ for all fitted curves). Residuals were calculated as the difference between the measured and fitted signals. Transient spike events were identified as positive deviations from the detrended residual signals and were defined as events exceeding both a relative detrended residual threshold of 0.02 and an absolute detrended residual threshold of 0.2 RFU. Spike activity was quantified as the number of detected events and the mean spike intensity, which was calculated from the absolute detrended residual amplitudes of the same detected spike events. For data visualization, OriginPro (version 2026, 10.3.0.197, OriginLab Corporation, Northampton, MA, USA) was used.

2.7. Fluorescence confocal microscopy

Fluorescence confocal microscopy was performed to visualize drug-rich domains in supersaturated samples. Samples were prepared as described for the Capflex experiments, including BODIPY 493/503 as a fluorescent tracer (20 nM, 1% v/v DMSO in PBS). Imaging was carried out using an Olympus Fluoview FV3000 confocal microscope (Olympus Corporation, Tokyo, Japan) equipped with a 20 × objective (NA 0.8). Excitation was performed at 488 nm, and emission was collected over the 500-600 nm range. Ritonavir (RTV), lopinavir (LPV), and loratadine (LRT) liquid samples at supersaturated concentrations of 25, 50, and 100 μM were imaged alongside corresponding blank sample (BODIPY 20 nM, 1% v/v DMSO in PBS) under identical acquisition settings.

3. Results and discussion

Building on the previously reported second harmonic scattering (SHS) platform (Kalasová et al., 2025), the present work used an upgraded version, now integrating linear light scattering (LLS) detection channel alongside SHS, while retaining the ultrafast laser source, to investigate a structurally diverse set of poorly water-soluble drugs (PWSDs). The platform was further optimised with respect to the optical detection geometry and expanded by implementing an LLS readout, enabling a simultaneous comparison of nonlinear and linear scattering responses. The measurements were designed to compare precipitation onset concentrations obtained from the two optical channels and to evaluate whether the combined response provides additional insight into aggregation processes occurring above the apparent solubility limit. Because SHS and LLS probe complementary physical properties, that is, interfacial symmetry and particle scattering contrast, respectively, a high similarity of the signals between the two readouts was not expected. Instead, differences between the channels were used as indicators of changes in aggregate symmetry, size, and internal organization during supersaturation.

Structurally diverse PWSDs were selected for this study. The molecular weight (Mw) ranged from 262 to 721 g/mol, spanning a range representative of marketed oral drugs (Shultz, 2019). The dataset comprised weakly acidic, basic, and neutral compounds, as well as representatives of all three glass-forming ability (GFA) classes.

Previous studies have reported incubation times for DMSO solvent-shift precipitation solubility assays ranging from minutes to two days (Sugano et al., 2006; Zhou et al., 2007). In this work, 1 h and 24 h were used to represent shorter and prolonged incubation conditions. The final DMSO concentration was maintained at 1% (v/v).

Table 1 summarizes the concentrations at which elevated scattering intensities were first observed in the LLS and SHS channels, together with the apparent solubility values obtained by reference HPLC method. The HPLC experiments followed the same solvent-shift protocol as the scattering measurements, with the only modification being an increase in sample volume from 100 to 200 μL to allow filtration before chromatographic analysis.

3.1. Linear light scattering versus reference chromatographic method

In most cases, LLS yielded onset concentrations that were lower than, or close to, the solubility values obtained by HPLC. To quantify the overall agreement, the LLS onset concentrations were correlated with the HPLC apparent solubilities on a log10 scale, excluding values below the HPLC quantification limit (Figure 2). Significant positive correlations were observed at both time points, with Pearson $r = 0.81$ ($R^2 = 0.65$, $p = 4.8 \times 10^{-3}$, $n = 10$) at 1 h and $r = 0.91$ ($R^2 = 0.84$, $p = 3.4 \times 10^{-5}$, $n = 12$) at 24 h, indicating good overall concordance despite the methodological differences between the two techniques. However, compound-specific deviations were observed and are discussed below.

LLS was used to detect the onset of optically detectable aggregation or precipitation, whereas HPLC quantified the drug concentration remaining after 0.22 μm filtration. The HPLC values should therefore be interpreted as apparent concentrations defined by the applied solvent-shift and filtration protocol, rather than as direct measurements of the exclusively molecularly dissolved fraction. This distinction is

Table 1
Concentration-dependent scattering onsets determined by linear light scattering (LLS) and second harmonic scattering (SHS), together with apparent solubility values obtained from the solvent-shift HPLC assay. Measurements were performed in PBS pH 7.4 with 1% (v/v) DMSO after 1 h and 24 h of incubation. Values are reported as mean ± standard deviation from three independent replicate series (n = 3). Ionization class: A = acidic, B = basic, N = neutral. GFA = glass-forming ability class.

Compound	Mw (g/mol)	Ionization class	GFA*	Time (h)	LLS (μM)	SHS (μM)	HPLC (μM)
Albendazole	265.3	B	III	1	2.1 ± 0.1	2.8 ± 0.2	1.8 ± 0.1
				24	1.7 ± 0.2	2.4 ± 0.3	1.1 ± 0.0
Bifonazole	310.4	B	II	1	4.3 ± 1.4	5.9 ± 0.3	<0.8***
				24	1.4 ± 0.1	5.9 ± 0.4	0.9 ± 0.1
Carbamazepine	236.3	N	III	1	517.8 ± 15.5	716.4 ± 39.3	334.7 ± 12.6
				24	301.1 ± 13.5	818.2 ± 12.9	466.7 ± 13.2
Carvedilol	406.5	B	III	1	31.9 ± 0.3	39.9 ± 2.4	143.9 ± 2.8
				24	125.2 ± 0.1	127.2 ± 0.5	72.5 ± 1.8
Dipyridamole	504.6	B	n.a.	1	13.5 ± 0.6	3.5 ± 0.9**	18.9 ± 0.4
				24	1.9 ± 0.1	1.9 ± 0.8	7.3 ± 0.2
Griseofulvin	352.8	N	III	1	115.6 ± 26.8	115.3 ± 16.9	82.6 ± 1.5
				24	32.1 ± 2.5	38.6 ± 7.0	46.2 ± 1.5
Haloperidol	375.9	B	I	1	8.5 ± 0.1	16.5 ± 1.2	43.1 ± 1.2
				24	31.8 ± 0.1	37.7 ± 3.3	38.0 ± 2.1
Lopinavir	628.8	N	III	1	1.3 ± 0.2	25.5 ± 2.4	13.7 ± 0.3
				24	1.4 ± 0.0	2.2 ± 0.3	10.9 ± 0.2
Loratadine	382.9	B	III	1	1.3 ± 0.0	5.5 ± 0.2	9.4 ± 0.2
				24	1.4 ± 0.0	1.4 ± 0.0	4.3 ± 0.5
Pimozide	461.6	B	II	1	0.2 ± 0.2	18.5 ± 2.5	< 0.8***
				24	0.1 ± 0.0	1.7 ± 0.1	1.2 ± 0.2
Ritonavir	720.9	B	III	1	1.4 ± 0.0	22.8 ± 1.0	37.4 ± 0.2
				24	1.4 ± 0.1	1.5 ± 0.2	11.7 ± 2.4
Tolfenamic acid	261.7	A	I	1	67.2 ± 8.5	95.8 ± 73.7	322.1 ± 5.1
				24	230.7 ± 34.3	199.1 ± 17.5	282.5 ± 10.2

* Data taken from (Baird et al., 2010; Blaabjerg et al., 2018; Wyttenbach et al., 2016; Wyttenbach and Kuentz, 2017), n.a. = not available.
** Spectral interference: dipyridamole fluorescence/background signal in the SHS detection channel near 515 nm contributed to the apparent SHS onset.
*** Below quantification limit

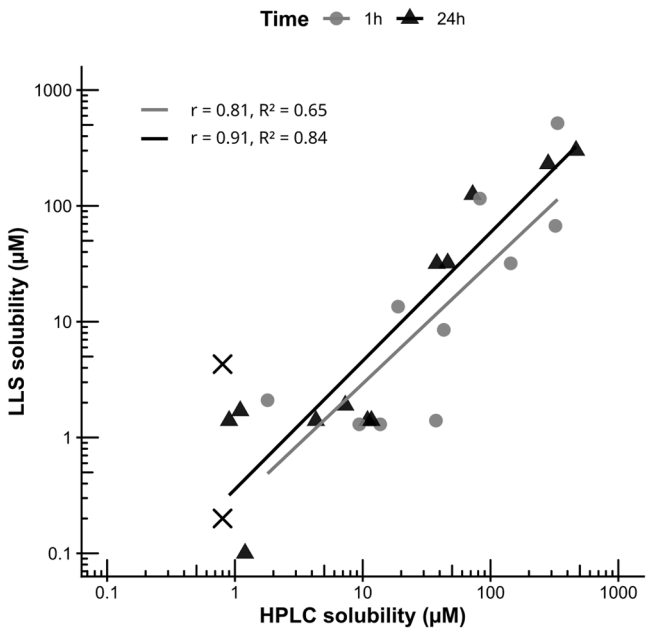

Figure 2. Correlation between the LLS-derived and HPLC-derived apparent solubilities at 1 h (grey circles) and 24 h (black triangles). Lines show log-log linear regression fits; Pearson r and R^2 values were calculated from log10-transformed data. Crosses indicate values excluded from the correlation due to HPLC results below the quantification limit.

particularly important in supersaturated systems, where colloid-associated or other submicron drug-rich species may remain in the filtrate and contribute to the measured concentration. Related work by Holzem et al. highlights the distinction between apparently dissolved, colloid-associated, and molecularly dissolved drug fractions in supersaturated systems, and illustrates the use of dedicated separation approaches, including microdialysis and nanofiltration, to differentiate these fractions (Holzem et al., 2023). In the present dataset, the HPLC-based apparent solubilities were mostly higher than the LLS-derived scattering onsets, which is consistent with LLS detecting the first appearance of scattering species, while HPLC quantifies the drug remaining in the filtrate after the applied separation step. In a few cases (bifonazole, carbamazepine, and griseofulvin at 1 h; carvedilol at 24 h), the LLS onset concentration slightly exceeded the corresponding HPLC value. Because these differences remained within the same order of magnitude, they likely reflect compound-specific and method-specific effects rather than a fundamental disagreement between the two techniques. For griseofulvin at 1 h, the discrepancy may additionally have been amplified by the coarser concentration spacing, as the LLS onset concentration was estimated within a relatively wide interval between the measured points of 62.5 and 125 µM.

For most compounds, particularly those classified as GFA class II and III, the apparent solubility at 1 h was comparable to or modestly higher than the corresponding value obtained at 24 h. This behaviour is characteristic of supersaturated systems, in which dissolved drug progressively relaxes toward equilibrium through nucleation and growth of a solid phase during prolonged incubation (Kawakami, 2017). This trend was observed for most compounds in the present dataset, except for carvedilol, haloperidol, and tolfenamic acid.

For carvedilol, the LLS onset remained lower at 1 h than at 24 h, even upon repeated measurements, whereas the HPLC results showed the opposite trend. The LLS and SHS scattering signals at low concentrations may have originated from submicron particles (that were not fully retained by the 0.22 µm filtration in the HPLC experiment) that were partially redissolved during incubation. The adsorption of material to the well plate surface during prolonged equilibration also cannot be excluded.

For haloperidol and tolfenamic acid (GFA class I compounds with rapid crystallization), the lower apparent onset concentrations observed at 1 h likely reflected transient submicron particles generated immediately after solvent shift. The samples were initially turbid but became optically clear after 24 h, suggesting redissolution of these particles as the system relaxed toward equilibrium solubility. This, in turn, led to a closer agreement between the 24 h LLS and HPLC values.

Characterization of the residual solid phase can provide useful complementary information, particularly for experiments with a minimal scale such as shake-flask solubility experiments. However, the present workflow was intentionally designed as a miniaturized, material-sparing solvent-shift assay, and the amount of precipitated material remaining after the experiment was typically only in the low-microgram range, which was insufficient for reliable X-ray powder diffraction or robust Raman-based solid-form analysis. For this reason, both the SHS-LLS and HPLC assays were designed using the same solvent-shift principle, the same final DMSO content, and incubation conditions, so that possible solid-state transformations would be expected to occur under both assay formats rather than being specific to only one method. Therefore, no specific residual solid form is assigned here; definitive bottom-phase characterization would require dedicated scaled-up experiments.

As with other scattering-based methods for determining precipitation onset, the absolute values depend critically on the accuracy of the prepared stock solutions and chemical purity of the investigated compounds. Incomplete dissolution in DMSO, weighing errors at small masses, or residual solid material in the stock, can introduce systematic shifts in the apparent onset concentration. In addition, trace impurities with distinct solubilities or optical properties may contribute disproportionately to the measured scattering signal, thus biasing the detected onset. Thus, the LLS onsets should be viewed as method-defined optical thresholds under the applied solvent-shift conditions, rather than absolute thermodynamic solubilities. Nonetheless, their broad qualitative agreement with independently determined HPLC-based solvent-shift solubility values for most compounds supports their practical relevance in identifying the earliest aggregation onsets in supersaturated systems.

3.2. *Sensitivity of the linear light scattering channel*

The analytical sensitivity of the LLS method is illustrated in Figure 3 using pimozide, which was selected as a showcase compound owing to its low onset concentration in this dataset. A reproducible increase in scattering intensity above the baseline was observed already at 0.1 µM, demonstrating that the method can resolve precipitation-related events in the sub-micromolar concentration range. The close agreement between the three independent replicate series further supported that the observed signal increase reflected genuine particle detection rather than random background noise.

For comparison, conventional nephelometric methods typically detect precipitation only at concentrations on the order of ~ 10 to 30 µM (Hoelke et al., 2009; Kramer et al., 2009; Wang and Matayoshi, 2012), whereas confocal static light-scattering approaches have reported detection limits in the range of ~ 0.1 to 0.2 µM (Wang and Matayoshi, 2012). The sensitivity observed here is therefore comparable to the most sensitive confocal nephelometric approaches while substantially exceeding that of standard nephelometric instruments. The platform also offers practical throughput, enabling scanning of a full 384-well plate in 15 minutes, which is compatible with high-throughput discovery workflows. The lowest onset concentrations observable with this method are inherently constrained by the solubility of the compounds investigated. Whether the ultrafast laser configuration permits detection of particle formation at concentrations below those observed here would require further investigation using compounds with even lower aqueous solubility and therefore remains to be determined.

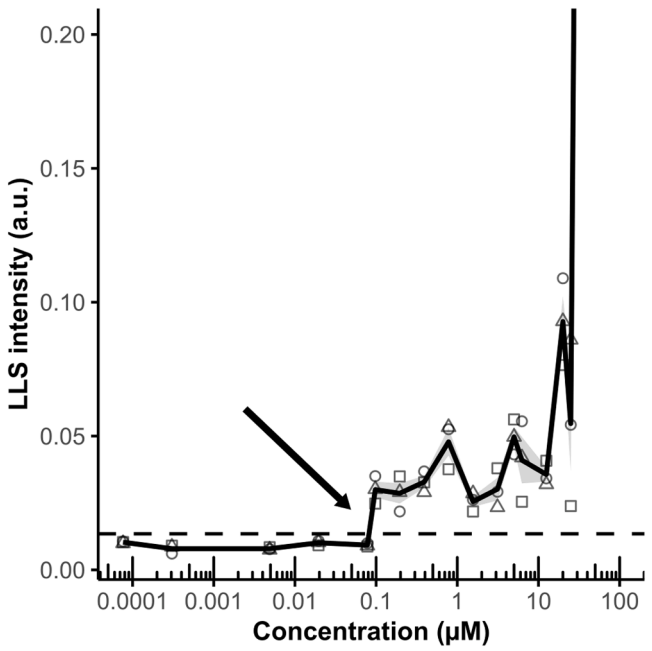

Figure 3. Demonstration of the high sensitivity of the scattering platform using an ultrafast laser. Linear light scattering (LLS) is shown as a function of pimozide concentration measured 24 h after preparation. The curve represents the averaged signal from three independent replicate sets, with the grey band indicating the standard deviation, and individual datapoints are shown for replicate series 1 (○), 2 (□), and 3 (△). The dashed line shows the averaged blank signal (1% v/v DMSO in PBS- pH 7.4; n = 287), and the black arrow indicates the onset of scattering associated with drug precipitation/aggregation.

3.3. Second harmonic scattering versus linear light scattering

Second harmonic scattering (SHS) and linear light scattering (LLS) report on different aspects of aggregation. SHS is highly sensitive to interfacial asymmetry and orientational order (Roke and Gonella, 2012; Tarun et al., 2025), whereas LLS responds primarily to particle size and refractive index contrast, and can be pushed to very low detection limits with an appropriate optical design (Maguire et al., 2018).

SHS onset concentrations were, in several cases, close to those obtained from the LLS channel, but systematic deviations were also observed (Table 1). Small offsets between the two channels were expected, because SHS and LLS data were evaluated independently and the onset in each case was defined relative to channel-specific baseline variability. Therefore, such minor discrepancies reflect variations in the respective thresholding criteria rather than meaningful differences in particle formation.

Dipyridamole was a compound-specific exception. Because it is coloured and exhibits fluorescence in the spectral region of the SHS detection channel (515 nm), the signal recorded at this wavelength cannot be attributed solely to second harmonic scattering. This spectral interference introduced a concentration-dependent background contribution to the SHS channel and led to an artificially lower apparent SHS onset concentration. The dipyridamole SHS onset should therefore be interpreted with caution and is not directly comparable to non-coloured compounds for mechanistic analysis.

Larger discrepancies were observed for carbamazepine at both time points; for haloperidol, lopinavir, loratadine, ritonavir, and tolfenamic acid after 1 h; and for pimozide at both 1 h and 24 h. In these cases LLS indicated particle formation at lower concentrations than SHS. This suggested that, in at least some systems, the earliest species formed after solvent shift were LLS-visible but SHS-weak: particles may have been very small, structurally close to isotropic spheres, or characterised by low effective second-order susceptibility, contributing little to coherent SHS signal while already producing measurable linear scattering (Chu et al., 2023; Tarun et al., 2025). In these cases, the SHS "onset" should therefore not be equated with the absolute onset of precipitation, but rather with the concentration at which interfacial asymmetry and/or nonlinear susceptibility have grown sufficiently to cross the SHS detection threshold.

Because the generation of second harmonic photons requires high peak excitation intensities, the platform used in this study employed an ultrafast pulsed laser source. The same excitation conditions were inherently applied to the LLS channel, where the high peak intensity (> 10 MW per pulse) improved the signal-to-noise and background suppression compared with conventional continuous-wave nephelometric approaches (average power ~ 100 mW), enabling the detection of very small particles or low particle concentrations at the early aggregation stages. For this dataset, the SHS onset thus marks the emergence of sufficiently asymmetric, SH-active interfaces, whereas LLS reports on the concentration at which particle formation first becomes optically detectable. This distinction was particularly evident for lopinavir, loratadine, and ritonavir, which showed delayed SHS onsets and complex concentration-dependent SHS profiles that were further investigated using orthogonal methods.

3.4. Peculiar SHS patterns

The LLS scattering onset concentrations provided a useful estimate of the solubility thresholds, qualitatively similar to HPLC-based measurements, whereas the combined SHS-LLS readout revealed additional concentration-dependent transitions for lopinavir (LPV), loratadine (LRT), and ritonavir (RTV), namely pronounced local peaks followed by attenuated intensity levels in the SHS response (Figure 4). Similar local maxima followed by reduced SHS intensity have previously been reported for sodium lauryl sulphate and were attributed to increased centrosymmetry upon micelle formation (Kalasová et al., 2025). The analogous patterns observed here for LPV, LRT, and RTV indicated the presence of structurally distinct mesoscale centrosymmetric structures forming above the solubility threshold, typically at degrees of supersaturation (DS) between approximately 4 and 40.

Figures 4A-C, together with the scattering profile classification in Figure 5, show that the corresponding LLS intensity-concentration profiles displayed a simpler two-regime behaviour. After deviation from baseline, the LLS signal entered an intermediate scattering regime (regime I), characterised by elevated but only weakly concentration-dependent intensity levels. In most cases, this regime manifested as a plateau preceding the pronounced signal increase observed in regime II at higher concentrations, where the samples contained a substantially increased population of scattering particles. In the Rayleigh regime, where particle dimensions are much smaller than the incident wavelength, the scattering intensity from a dispersion scales with particle number density and with the Rayleigh cross section, which depends on particle radius and refractive-index contrast with medium. As the particle size increases to dimensions comparable to the wavelength (size parameter x ~ 1), the Rayleigh approximation breaks down, and Mie/transition-regime effects appear; larger particles then contribute disproportionately to the total scattering, leading to a stronger increase in the measured intensity (Galy et al., 2020; Gautam et al., 2024). Accordingly, regime I described here is aligned with the presence of small scattering entities whose size remains approximately constant while their number density increases, whereas regime II reflects particle growth and the emergence of larger precipitates that dominate the scattering response.

In contrast to the two-regime evolution of the LLS signal, the SHS response displayed a characteristic peak-drop-rise pattern. After 24 h of equilibration, pronounced SHS local maxima were observed between 1.6 and 12.5 μM for LPV, between 1.3 and 5.0 μM for LRT, and between 1.3 and 6.3 μM for RTV. These peaks occurred close to the concentration range where the LLS signal first deviated from the baseline, consistent

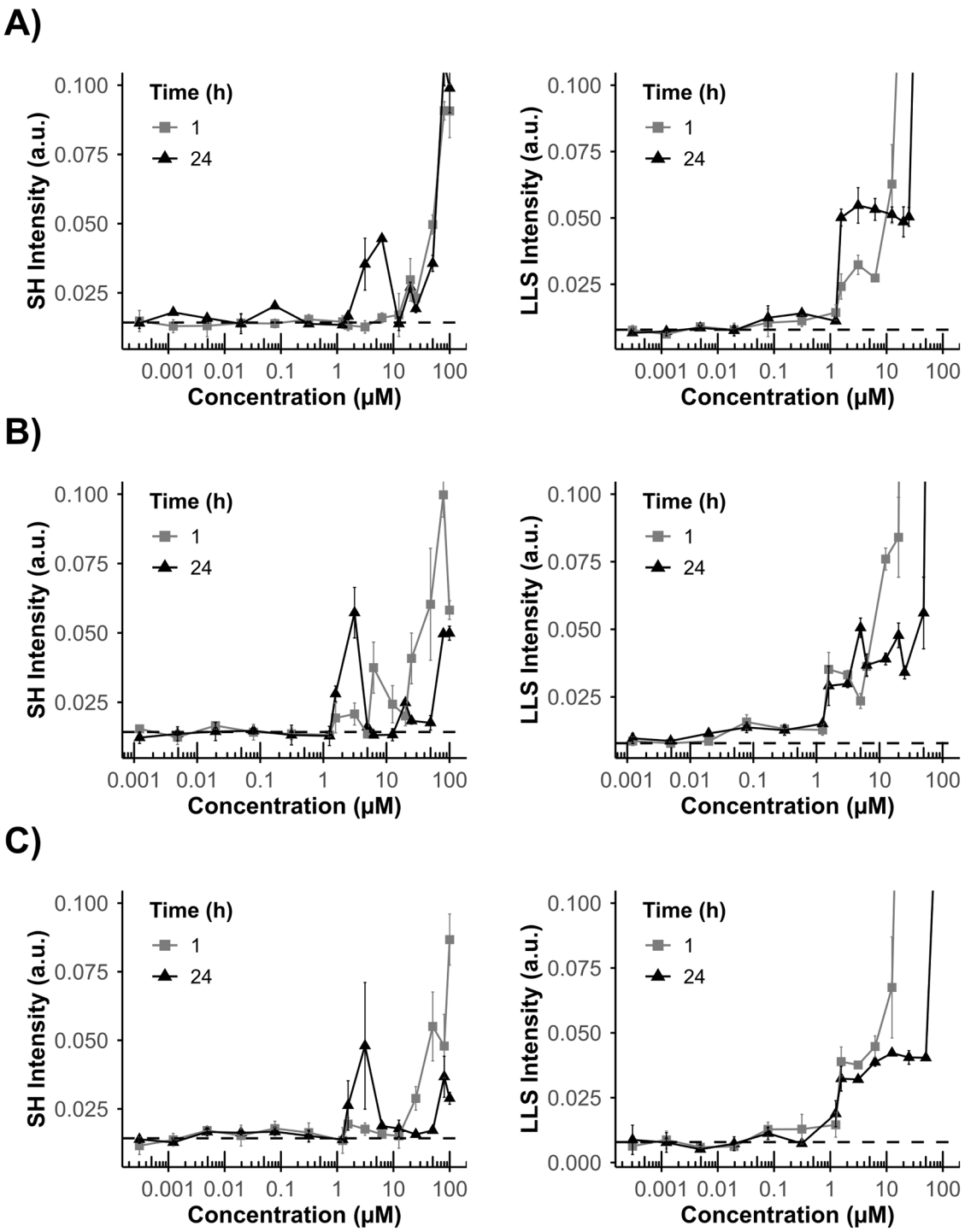

Figure 4. Concentration-dependent second harmonic scattering (SHS; left panels) and linear light scattering (LLS; right panels) intensities using an ultrafast laser for A) lopinavir, B) loratadine, and C) ritonavir after 1 h (grey, ■) and 24 h (black, ▲) after sample preparation. Data are shown as mean values from three independent replicate series, with error bars representing the standard deviation. The dashed line indicates the averaged blank signal (1% (v/v) DMSO in PBS pH 7.4; n = 287).

with SHS being sensitive to nanoscale interfacial fluctuations and aggregation phenomena near the solubility limit (Kalasová et al., 2025; Tarun et al., 2025). At higher concentrations above these local maxima (approximately DS ≈ 4 to 40), the SHS signal decreased toward baseline, whereas the LLS response remained elevated within regime I. This contrast between the two channels indicated the formation of scattering entities that contributed to linear scattering but had a limited effective second-order nonlinear response, for example due to increased centrosymmetry or reduced interfacial polarity/orientational order (Chu et al., 2023; Roke and Gonella, 2012).

Based on the SHS selectivity for non-centrosymmetric, interfacial structures and its known sensitivity to aggregation and supramolecular organization, it is hypothesised that the reduced SHS signal in this concentration range arose from drug-rich domains (in either liquid or glassy form), whose interfaces generated only a weak effective second-order susceptibility due to their relatively low interfacial asymmetry or partially centrosymmetric molecular arrangement (Chu et al., 2023; Roke and Gonella, 2012). Although the present optical measurements do

Drug	Conc. range (μM)	1 h		24 h	
		SHS	LLS	SHS	LLS
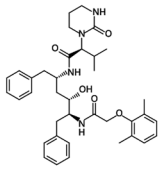 Lopinavir	0.0-1.3	baseline	baseline	baseline	baseline
	1.3-1.6		regime I		regime I
	1.6-6.3			local peak	
	6.3-12.5		regime II		
	12.5-25.0	attenuated		attenuated	
	25.0-100.0	rise		rise	regime II
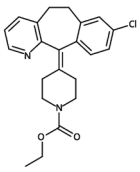 Loratadine	0.0-1.3	baseline	baseline	baseline	baseline
	1.3-5.0	local peak 1*	regime I	local peak	regime I
	5.0-6.3	local peak 2		attenuated	
	6.3-20.0		regime II		
	20.0-50.0	rise			
	50.0-100.0			weak rise	regime II
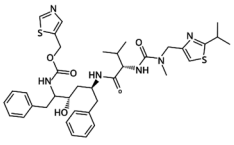 Ritonavir	0.0-1.3	baseline	baseline	baseline	baseline
	1.3-6.3		regime I	local peak	regime I
	6.3-12.5		regime II	attenuated	
	12.5-50.0	rise			
	50.0-100.0			weak rise	regime II

*Below 3σ upper limit

Figure 5. Graphical tabulation of concentration-dependent SHS and LLS scattering regimes for lopinavir, loratadine, and ritonavir measured 1 h and 24 h after the sample preparation. The regime assignments summarize the qualitative scattering behaviour observed across concentration ranges.

not directly resolve molecular-scale pathways, this interpretation is conceptually consistent with non-classical, multistep nucleation models in which dense, disordered, or liquid-like precursor clusters may precede subsequent structural ordering into a crystalline phase (Zahn, 2015). Upon further concentration increase, the transition to regime II in the LLS channel was accompanied by a modest recovery of the SHS signal, indicating the formation of larger precipitates and increased interfacial area. However, this increase remained comparatively weak for LRT and RTV relative to the 1 h measurements, while for LPV the SHS intensity at higher concentrations remained essentially unchanged.

Second-order nonlinear imaging of chiral crystals (SONICC) and second harmonic generation (SHG) studies in pharmaceutical solids show that crystalline drug domains embedded in largely amorphous matrices generate strong SHG signals, whereas amorphous components provide negligible background and are effectively SHG-silent (Kestur et al., 2012; Mastalieva et al., 2024). More generally, in nanocomposite and nanoconfined systems, SHG arises predominantly from non-centrosymmetric crystalline regions, while disordered or amorphous shells do not contribute measurably to the SHG signal (El Karout et al., 2023; Tilmann et al., 2023).

Considering this literature, the comparatively weak SHS recovery for LRT and RTV is consistent with precipitates whose interfaces generate only a small effective second-order response. It is therefore hypothesised that the precipitates at the highest concentrations for LRT and RTV were predominantly amorphous or contained only limited non-centrosymmetric crystalline regions, leading to a reduced SHS signal compared with more strongly crystalline precipitates/aggregates.

For LPV after 1 h, the onset of a significant SHS response was observed only at 25.5 μM, i.e. at concentrations where the LLS signal had already transitioned into regime II. Between 12.5 and 25 μM, only weak SHS signals were recorded, remaining below the 3σ detection threshold. One possible interpretation is the presence of a dynamically evolving population of drug-rich domains or nanoscale amorphous aggregates generated shortly after the solvent shift, which scatter efficiently in LLS but remain only weakly SH-active owing to their small size or largely isotropic organization.

For LRT, a weak local SHS feature was already apparent between 1.3 and 5.0 μM at 1 h, although it remained below the 3σ threshold. After 24 h, this feature developed into a pronounced SHS maximum, indicating that the scattering species near the solubility boundary acquired a stronger interfacial second-order response during equilibration. The additional SHS peak observed after 1 h between 5.0 and 20 μM likely reflected a transient, non-equilibrium population formed shortly after solvent shift, which reorganised upon prolonged incubation and no longer produced a strong SHS response after 24 h.

For RTV at 1 h, no distinct intermediate SHS maximum was detected. Although the LLS signal entered regime II above 6.3 μM, the SHS intensity remained near the baseline until approximately 12.5 μM, with the 3σ onset determined at 22.8 μM, pointing to predominantly isotropic or amorphous precipitates at short equilibration times.

To further investigate the origin of these intermediate SHS features, selected systems were examined using complementary orthogonal techniques, including scanning electron microscopy (SEM), fluorescence confocal microscopy, and capillary flow experiments (Capflex) based on Taylor dispersion, as described in Section 3.5.

3.5. Orthogonal characterization supporting the interpretation of the SHS patterns

To further examine the origin of the concentration-dependent SHS patterns, selected LPV, LRT, and RTV samples were investigated using orthogonal methods sensitive to particle morphology, dye partitioning, and droplet-like behaviour. Highly supersaturated aqueous solutions of these compounds have previously been reported to undergo liquid-liquid phase separation (LLPS) and form non-crystalline, drug-rich colloidal droplets or amorphous phases once the amorphous (metastable) solubility is exceeded (Ilevbare and Taylor, 2013; Indulkar et al., 2019; Trasi and Taylor, 2015). Therefore, SEM, Capflex, and confocal fluorescence microscopy were employed to assess whether the scattering features observed here could be associated with such non-classical precipitation pathways, involving drug-rich liquid-like, amorphous, or glassy precursor domains.

3.5.1. Scanning electron microscopy of precipitates

Scanning electron microscopy (SEM) was used to examine the morphology of the particles obtained after solvent-shift precipitation and to aid in the interpretation of the SHS patterns. Samples were prepared using the same solvent-shift protocol as for the SHS-LLS precipitation assay, except that ultrapure water replaced the buffer to avoid salt crystallization artefacts.

Marked compound-dependent differences in morphology were observed. LPV (Figure 6A), LRT (Figure 6B), and RTV (Figure 6C) predominantly yielded spherical features rather than faceted crystals. In contrast, HLP (Figure 6D), selected as a reference with fast crystallization kinetics, formed well-defined faceted structures consistent with direct crystallization from supersaturated solution.

Energy-dispersive X-ray spectroscopy revealed a strong carbon signal in the droplet-like structures, suggesting the presence of carbon-rich organic material (data not shown). In addition, the same preparation protocol applied to other compounds from this dataset led mostly to crystalline deposits (Supplementary Figure S1), suggesting that the spherical morphology was not simply a generic drying artefact. However, because the samples were dried before SEM imaging, the origin of these spherical structures must be interpreted with caution. Incomplete removal of residual solvent, including 1% (v/v) DMSO, cannot be fully excluded as a contributing factor.

The persistence of spherical, non-faceted structures for LPV, LRT, and RTV therefore suggests a compound-specific precipitation pathway, potentially involving transient drug-rich dense liquid or amorphous domains, as reported for other small-molecule systems undergoing LLPS or two-step nucleation (Guo et al., 2016; Ilevbare and Taylor, 2013; Tres et al., 2018b). While SEM cannot directly confirm LLPS due to possible drying-induced transformation or vitrification, these observations motivated further investigation using solution-phase methods (Capflex, confocal microscopy) that are better suited to probe particle structures without drying artefacts.

3.5.2. Capillary flow experiments (Capflex) to detect LLPS

Flow-induced dispersion analysis (FIDA) is a capillary-based fluorescence technique originally developed to quantify ligand binding via changes in the apparent hydrodynamic radius of a fluorescent indicator extracted from Taylor dispersion profiles (Jensen and Østergaard, 2010). More recently, the same instrument platform has been adapted as Capflex, a capillary flow method for quantitative analysis of LLPS, in which transient fluorescence spikes generated by tracer-enriched droplets are used to detect separating phase and to determine dilute-phase concentrations (Stender et al., 2021). In parallel, environment-sensitive fluorescent probes have been used to identify drug-rich phases in supersaturated solutions of PWSDs, based on preferential partitioning of the probes into nonpolar, drug-rich aggregates formed by LLPS (Raina et al., 2015; Tres et al., 2018a).

In the present study, the Capflex method was used to probe drug-rich domains formed upon supersaturation of HLP, LPV, LRT, and RTV. BODIPY 493/503 (20 nM) served as a hydrophobic tracer expected to preferentially partition into nonpolar drug-rich droplets, if present. Under these conditions, the intermittent passage of dye-enriched domains through the detection volume produced discrete fluorescence spikes in the signal trace, analogous to droplet spikes as observed in protein LLPS experiments (Stender et al., 2021). Representative Capflex fluorescence-time traces for LPV after 1 h of equilibration are shown in Figure 7, while quantitative summaries of spike counts and mean spike intensities for HLP, LPV, LRT, and RTV are presented in Figure 8. The complete fluorescence-time trace series for all four compounds after 1 and 24 h of equilibration is provided in Supplementary Figure S2.

HLP, a fast-crystallizing (GFA class I) compound that was not expected to undergo LLPS, was included as a negative control. In line with this assumption, only few, low-intensity spikes were detected over the studied concentration range. Occasional spikes at higher concentrations may reflect sporadic co-precipitation or surface adsorption events involving the dye and solid particles, rather than a stable population of drug-rich droplets.

For LPV, fluorescence spikes were consistently observed at concentrations $\geq$ 40 μM. Among all the investigated drugs, LPV produced the highest spike intensities, indicative of dye-enriched mesoscale assemblies. Spike occurrence was most frequent at 50 μM, whereas individual spikes became more intense at 75 and 100 μM, consistent with a shift from numerous smaller domains to fewer, larger, or more dye-enriched domains at increasing supersaturation. After 24 h, spikes were still observed, but the mean spike intensity decreased at concentrations $\geq$ 50 μM compared with 1 h. This suggested a time-dependent evolution of the fluorescent domains and may reflect changes in size, dye partitioning, or partial conversion into less dye-enriched solid material. Because the capillary had an inner diameter of 75 μm, aspiration of solid particles or aggregates smaller than this cannot be excluded. Therefore, some fluorescence spikes may also originate from solid particles onto which BODIPY adsorbed or with which it co-precipitated, rather than exclusively from liquid-like droplets.

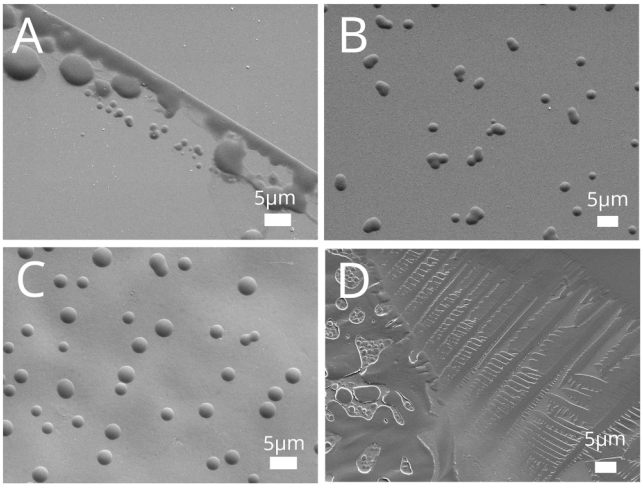

Figure 6. Scanning electron microscopy (SEM) images of particles obtained after solvent-shift precipitation in water for A) lopinavir (LPV, 100 μM), B) loratadine (LRT, 100 μM), C) ritonavir (RTV, 100 μM), and D) haloperidol (HLP, 500 μM). The concentration values in parentheses indicate the target nominal drug concentrations after dilution.

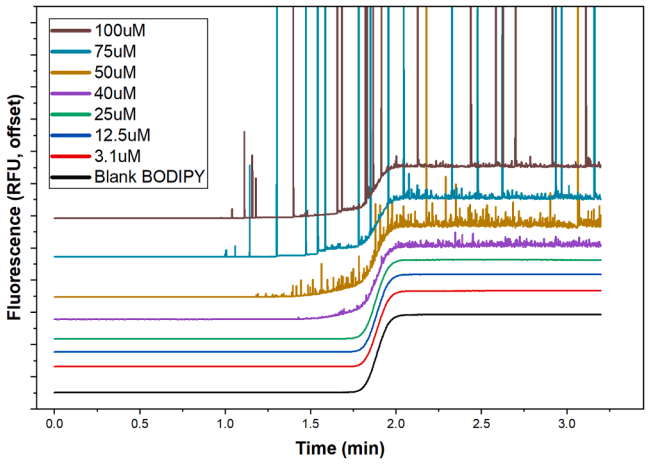

Figure 7. Capflex fluorescence-time traces for lopinavir (LPV) samples prepared at increasing concentrations using the solvent-shift method (1% v/v DMSO, PBS) and equilibrated for 1 h. Samples contained 20 nM BODIPY 493/503 as a hydrophobic fluorescent tracer for drug-rich domains. Intermittent fluorescence spikes indicate the transient passage of BODIPY-enriched domains through the detection volume. Traces are vertically offset for clarity.

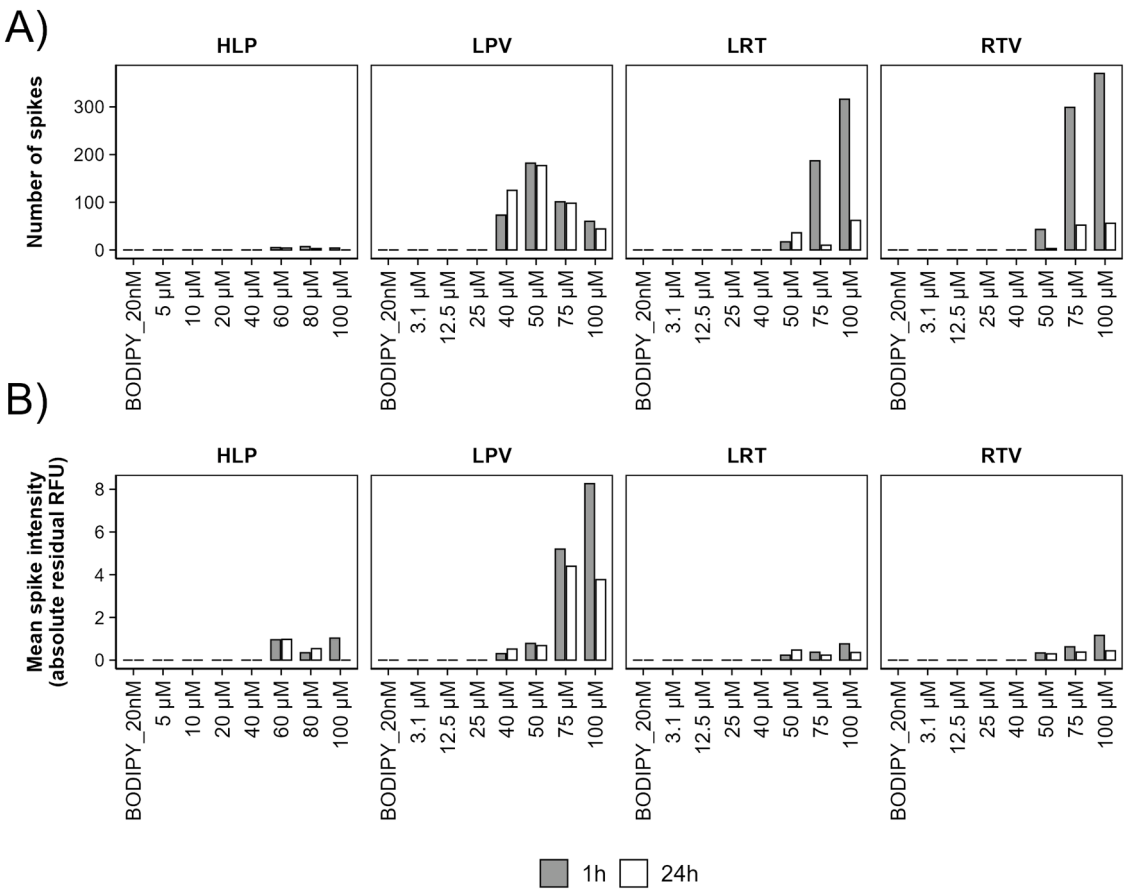

Figure 8. Quantitative Capflex analysis of drug-rich domains based on partitioning of the fluorescent tracer BODIPY 493/503. Samples contained 20 nM BODIPY 493/503 and increasing drug concentrations, as indicated on the x-axis. Bar plots show A) the number of fluorescence spikes and B) the mean spike intensity for the negative control haloperidol (HLP) and the compounds lopinavir (LPV), loratadine (LRT), and ritonavir (RTV) after 1 h (grey bars) and 24 h (white bars) of equilibration. The BODIPY-only sample represents the tracer control without drug.

For LRT and RTV, spikes emerged at concentrations $\geq$ 50 µM. In contrast to LPV, these samples showed higher spike frequencies but lower mean spike intensities, suggesting the presence of a larger population of smaller dye-loaded domains at comparable supersaturation. Both spike count and spike intensity decreased substantially after 24 h incubation, indicating progressive depletion of these metastable drug-rich domains, most likely through conversion into more stable crystalline or amorphous solid material, as expected for non-equilibrium liquid-like phases. Notably, residual spikes were still detected after prolonged incubation, indicating that a fraction of the drug-rich domains persisted even after partial precipitation. This was in qualitative agreement with confocal fluorescence microscopy, which likewise revealed a small number of remaining droplets after 24 h.

3.5.3. Fluorescent confocal microscopy

Finally, confocal fluorescence microscopy (Figure 9) was used to visualize BODIPY-enriched drug structures formed after solvent-shift for RTV, LPV, and LRT, analogous to the Capflex analysis described above. A blank control containing 20 nM BODIPY 493/503 in the absence of drug showed only diffuse fluorescence and no droplet-like objects (Supplementary Figure S3), indicating that the observed fluorescent droplets/precipitates were not caused by self-association of the dye alone.

For RTV, fluorescent droplets with diameters on the order of $\sim$ 1 µm were observed at 50 µM shortly after preparation, whereas no droplets were detected at lower concentrations. After 24 h, the droplets were still present, although their number was reduced. This indicated that RTV formed drug-rich domains rapidly after the solvent shift and that a fraction of these domains persisted over prolonged equilibration.

For LPV, fluorescent droplets were also observed at 50 µM immediately after preparation. Some structures showed apparent elongation, which was attributed to droplet motion during image acquisition, and coalescence events were visible, consistent with liquid-like behaviour. No droplets were observed below this concentration in this experiment. After 24 h, the fluorescent signal was predominantly associated with irregular particle-like structures rather than clearly resolved droplets, suggesting the progressive conversion of the initial drug-rich domains into more solid material, with BODIPY likely being incorporated into or adsorbed onto the precipitated drug phase.

For LRT, no clear droplets were observed at 50 µM and below, whereas at 100 µM, numerous fluorescent droplet-like structures were detected shortly after preparation, with evidence of coalescence into larger assemblies. After 24 h, a substantial fraction of the visible particles appeared non-fluorescent by observation, whereas a small number of fluorescent droplets of approximately 1 µm remained. These results were consistent with the Capflex measurements, which already detected spikes at $\geq$ 50 µM but with relatively low mean intensities, suggesting the presence of very small drug-rich domains likely below the detection limit of confocal microscopy. At 100 µM, the frequent appearance of non-fluorescent precipitates indicated that the highly supersaturated drug was partly converted into solid material, while a residual tendency toward LLPS persisted, as reflected by the remaining fluorescent droplets and Capflex spike signals.

Together, the confocal microscopy data supported concentration-dependent formation of drug-rich, BODIPY-enriched domains for RTV, LPV, and LRT. The concentration thresholds at which droplets became

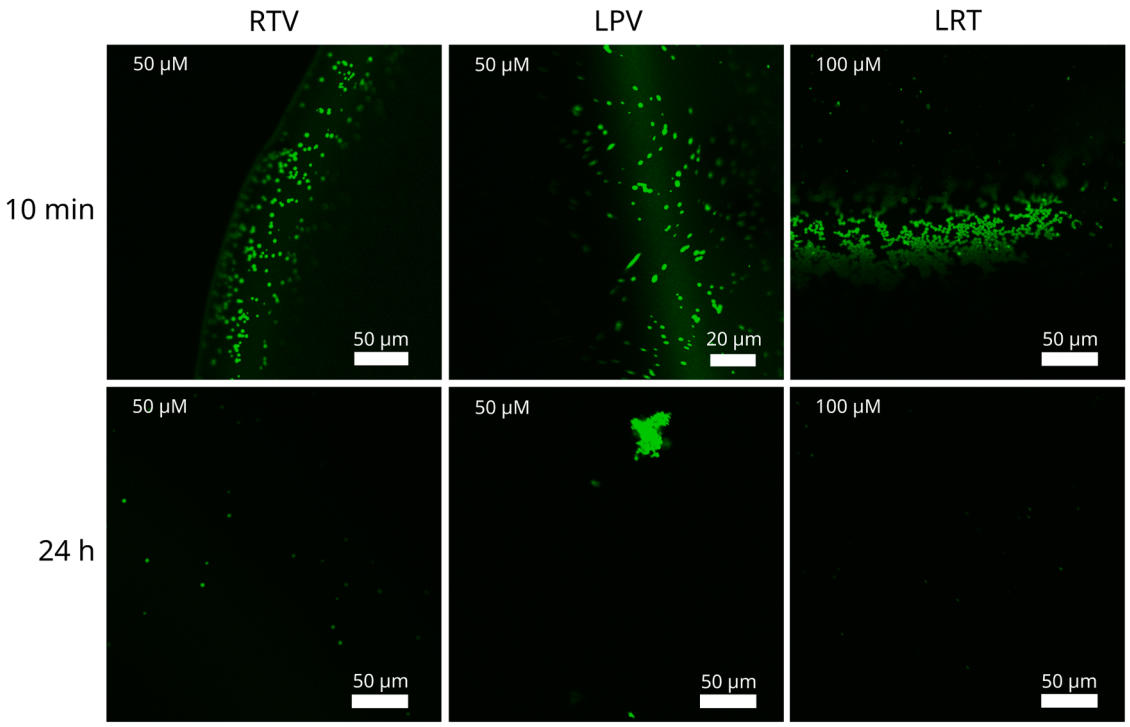

Figure 9. Confocal fluorescence microscopy images of supersaturated liquid samples prepared by DMSO solvent shift in PBS (pH 7.4; final DMSO content 1% v/v) containing BODIPY 493/503 (20 nM) as a hydrophobic fluorescent tracer. Columns show ritonavir (RTV, 50 μM), lopinavir (LPV, 50 μM), and loratadine (LRT, 100 μM), respectively. Images acquired within 10 min after preparation are shown in the top row, while images recorded after 24 h of equilibration are shown in the bottom row.

visible were broadly consistent with the Capflex measurements, although direct comparison should be made cautiously because the confocal images were recorded within 10 min of preparation, whereas the main Capflex dataset was collected after 1 h.

3.6. Interpretation of attenuated SHS regimes supported by orthogonal characterization

The orthogonal techniques employed in this study (SEM, Capflex, and confocal fluorescence microscopy) provided complementary evidence for drug-rich mesoscale assemblies in LPV, LRT, and RTV samples and helped interpret the attenuated SHS regimes observed above the apparent solubility but below the onset of pronounced precipitation-dominated scattering. Confocal fluorescence microscopy did not reveal droplet-like structures below 50 μM. Given the diffraction-limited spatial resolution of confocal laser scanning microscopy and the known nanoscale size of LLPS-derived drug-rich droplets, this lack of visible droplets was most plausibly consistent with an optical detection limit rather than evidence for their absence. Consistently, Capflex fluorescence spikes were detected only at higher concentrations, $\geq$ 40 μM for LPV and $\geq$ 50 μM for LRT and RTV, broadly matching the concentration range in which fluorescent assemblies became visible by confocal microscopy. This comparison should, however, be interpreted with caution because the measurements correspond to different equilibration times, approximately 10 min for confocal microscopy and 1 h for Capflex. In addition, the Capflex method itself is also subject to a practical lower size sensitivity, because droplets substantially smaller than the detection volume will generate only weak, noisy or undetectable spikes.

Together, these observations indicate that LPV, LRT, and RTV can form drug-rich droplet-like or amorphous precursor domains prior to pronounced precipitation, as supported by fluorescence spikes in Capflex experiments, spherical morphologies observed by SEM after drying, and fluorescent assemblies detected by confocal microscopy. Although these features became directly detectable only at higher concentrations than those corresponding to the attenuated SHS regimes, they support a compound-specific tendency to form dense drug-rich precursor phases upon supersaturation. At lower supersaturations, the attenuated SHS response is therefore most consistent with smaller nanoscale drug-rich assemblies that remain below the direct detection limits of the orthogonal methods. Their physical state cannot be assigned unambiguously and may correspond to nanoscale liquid-like droplets, dense amorphous clusters, or glassy aggregates. This interpretation is in line with reports of nanoscale drug-rich phases in supersaturated systems characterised using fluorescence-based methods, nanoparticle tracking analysis, ultracentrifugation, UV extinction/scattering, and related techniques (Indulkar et al., 2016; Purohit et al., 2017; Tres et al., 2018b).

4. Conclusion

An upgraded SHS platform equipped with a LLS channel allowed the simultaneous monitoring of complementary signatures of drug aggregation in supersaturated solutions in a miniaturised screening format. LLS, which reports on changes in particle size and number density (Maguire et al., 2018), was highly sensitive to the onset of precipitation, detecting particle formation at concentrations close to independently determined HPLC-derived apparent solubility limits across structurally diverse PWSDs. In contrast, SHS responded to the development of interfacial asymmetry and changes in nonlinear optical susceptibility (Chu et al., 2023; Roke and Gonella, 2012), yielding signals that were in several cases offset from the LLS onset and thus provided mechanistic information rather than redundant detection.

The combined SHS-LLS readout revealed that particle formation in supersaturated systems is not a single-step process but involves distinct intermediate regimes. In particular, for LPV, LRT, and RTV, a characteristic SHS peak-drop-rise pattern was observed, which was decoupled from the simpler two-regime LLS response. This behaviour was hypothesised to arise from transient drug-rich domains that were

detectable by LLS but exhibited a weak second-order nonlinear response, likely due to their small size, isotropic structure, or limited interfacial order (Chu et al., 2023; Roke and Gonella, 2012; Tarun et al., 2025).

Orthogonal characterization (SEM, Capflex, and confocal fluorescence microscopy) supported this interpretation by providing independent evidence for the formation of droplet-like or amorphous drug-rich assemblies prior to crystallization. While these domains became directly observable only at higher supersaturations, their presence at lower concentrations was strongly suggested by the SHS attenuation regimes, indicating nanoscale precursor phases such as liquid-like droplets, amorphous clusters, or glassy aggregates.

Overall, the data indicated that combining SHS with LLS enabled highly sensitive detection of incipient precipitation/aggregation events. Simultaneously, it provided access to structural and symmetry information that conventional techniques could not resolve, offering a powerful approach to study solubility, supersaturation, and phase transformation pathways in pharmaceutical systems on a miniaturised screening format.

Funding and role of funding source

This project received funding from the European Union's HORIZON-EIC-2023-TRANSITION-01 research and innovation programme under grant agreement No. 101159068 and from the Swiss Confederation Federal Department of Economic Affairs, Education and Research EAER State Secretariat for Education, Research and Innovation SERI.

Declaration of generative AI and AI-assisted technologies in the writing process

During the preparation of this manuscript, the authors used ChatGPT (OpenAI) to support language editing and to improve the clarity of the abstract, graphical abstract, and selected sections of the manuscript. The authors also used Consensus (Consensus NLP) to support the literature search and for identification of relevant publications. All AI-assisted outputs, literature suggestions, references, and scientific content were carefully reviewed and verified by the authors, revised where necessary, and the authors take full responsibility for the final content of the published article.

CRediT authorship contribution statement

Jitka Kalasová: Writing – original draft, Visualization, Validation, Methodology, Investigation, Formal analysis, Data curation, Conceptualization. **Orly Tarun:** Writing – review & editing, Funding acquisition, Conceptualization. **Martin Kuentz:** Writing – review & editing, Supervision, Resources, Funding acquisition, Conceptualization.

Declaration of competing interest

Orly Tarun is the CEO of Oryl Photonics SA, but otherwise the authors declare that they have no known competing financial interests that could have appeared to influence the work reported in this paper.

Acknowledgements

The authors gratefully acknowledge Vitali Helzer for his assistance with the scanning electron microscopy measurements.

Supplementary materials

Supplementary material associated with this article can be found, in the online version, at doi:10.1016/j.ejps.2026.107624.

Data availability

Data will be made available on request.

Reference

Alsenz, J., Kansy, M., 2007. High throughput solubility measurement in drug discovery and development. Adv. Drug Deliv. Rev. 59, 546–567. https://doi.org/10.1016/j.addr.2007.05.007.

Baird, J.A., Van Eerdenbrugh, B., Taylor, L.S., 2010. A classification system to assess the crystallization tendency of organic molecules from undercooled melts. J. Pharm. Sci. 99, 3787–3806. https://doi.org/10.1002/jps.22197.

Bhalani, D.V., Nutan, B., Kumar, A., Singh Chandel, A.K., 2022. Bioavailability Enhancement Techniques for Poorly Aqueous Soluble Drugs and Therapeutics. Biomedicines. https://doi.org/10.3390/biomedicines10092055.

Blaabjerg, L.I., Lindenberg, E., Löbmann, K., Grohganz, H., Rades, T., 2018. Is there a correlation between the glass forming ability of a drug and its supersaturation propensity? Int. J. Pharm. 538, 243–249. https://doi.org/10.1016/j.ijpharm.2018.01.013.

Chu, B., Marchioro, A., Roke, S., 2023. Size dependence of second-harmonic scattering from nanoparticles: Disentangling surface and electrostatic contributions. J Chem Phys 158. https://doi.org/10.1063/5.0135157.

Di, L., Fish, P.V., Mano, T., 2012. Bridging solubility between drug discovery and development. Drug Discov. Today. https://doi.org/10.1016/j.drudis.2011.11.007.

Di, L., Kerns, E.H., 2006. Biological assay challenges from compound solubility: strategies for bioassay optimization. Drug Discov. Today. https://doi.org/10.1016/j.drudis.2006.03.004.

El Karout, H., Shchur, Y., Andrushchak, A., Sahraoui, B., Wielgosz, R., Kityk, O., Jędryka, J., Slyvka, Y., Kityk, A.V., 2023. Second harmonic generation on crystalline organic nanoclusters under extreme nanoconfinement in functionalized silica–benzil composites. Sci. Rep. 13. https://doi.org/10.1038/s41598-023-37147-4.

Galy, T., Huang, D., Pilon, L., 2020. Revisiting independent versus dependent scattering regimes in suspensions or aggregates of spherical particles. J. Quant. Spectrosc. Radiat. Transf. 246. https://doi.org/10.1016/j.jqsrt.2020.106924.

Gautam, P., Moosmüller, H., Maughan, J.B., Sorensen, C.M., 2024. Light scattering from spherical and irregular particles over a wide angular range. Aerosol Science and Technology 58, 1053–1062. https://doi.org/10.1080/02786826.2024.2338543.

Guo, C., Wang, J., Li, J., Wang, Z., Tang, S., 2016. Kinetic Pathways and Mechanisms of Two-Step Nucleation in Crystallization. Journal of Physical Chemistry Letters 7, 5008–5014. https://doi.org/10.1021/acs.jpclett.6b02276.

Hoelke, B., Gieringer, S., Arlt, M., Saal, C., 2009. Comparison of nephelometric, UV-spectroscopic, and HPLC methods for High-throughput determination of aqueous drug solubility in microtiter plates. Anal. Chem. 81, 3165–3172. https://doi.org/10.1021/ac9000089.

Holzem, F.L., Jensen, I.H., Petrig Schaffland, J., Stillhart, C., Brandl, M., Bauer-Brandl, A., 2023. Combining in vitro dissolution/permeation with microdialysis sampling: Capabilities and limitations for biopharmaceutical assessments of supersaturating drug formulations. European Journal of Pharmaceutical Sciences 188. https://doi.org/10.1016/j.ejps.2023.106533.

Ilevbare, G.A., Taylor, L.S., 2013. Liquid-liquid phase separation in highly supersaturated aqueous solutions of poorly water-soluble drugs: Implications for solubility enhancing formulations. Cryst. Growth Des. 13, 1497–1509. https://doi.org/10.1021/cg301679h.

Indulkar, A.S., Gao, Y., Raina, S.A., Zhang, G.G.Z., Taylor, L.S., 2016. Exploiting the Phenomenon of Liquid-Liquid Phase Separation for Enhanced and Sustained Membrane Transport of a Poorly Water-Soluble Drug. Mol. Pharm. 13, 2059–2069. https://doi.org/10.1021/acs.molpharmaceut.6b00202.

Indulkar, A.S., Lou, X., Zhang, G.G.Z., Taylor, L.S., 2019. Insights into the Dissolution Mechanism of Ritonavir-Copovidone Amorphous Solid Dispersions: Importance of Congruent Release for Enhanced Performance. Mol. Pharm. 16, 1327–1339. https://doi.org/10.1021/acs.molpharmaceut.8b01261.

Jensen, H., Østergaard, J., 2010. Flow induced dispersion analysis quantifies noncovalent interactions in nanoliter samples. J. Am. Chem. Soc. 132, 4070–4071. https://doi.org/10.1021/ja100484d.

Kalasová, J., Tarun, O., Shynkarenko, Y., Kuentz, M., 2025. High-throughput analysis of aqueous drug solubility, supersaturation, and aggregation behaviour using second harmonic light scattering. Int. J. Pharm. 685. https://doi.org/10.1016/j.ijpharm.2025.126200.

Kawakami, K., 2017. Supersaturation and crystallization: non-equilibrium dynamics of amorphous solid dispersions for oral drug delivery. Expert Opin. Drug Deliv. https://doi.org/10.1080/17425247.2017.1230099.

Kestur, U.S., Wanapun, D., Toth, S.J., Wegiel, L.A., Simpson, G.J., Taylor, L.S., 2012. Nonlinear optical imaging for sensitive detection of crystals in bulk amorphous powders. J. Pharm. Sci. 101, 4201–4213. https://doi.org/10.1002/jps.23280.

Kramer, C., Heinisch, T., Fligge, T., Beck, B., Clark, T., 2009. A consistent dataset of kinetic solubilities for early-phase drug discovery. ChemMedChem 4, 1529–1536. https://doi.org/10.1002/cmdc.200900205.

Maguire, C.M., Rösslein, M., Wick, P., Prina-Mello, A., 2018. Characterisation of particles in solution–a perspective on light scattering and comparative technologies. Sci. Technol. Adv. Mater. https://doi.org/10.1080/14686996.2018.1517587.

Mastalieva, V., Neplokh, V., Aybush, A., Stovpiaga, E., Eurov, D., Vinnichenko, M., Karaulov, D., Kirillenko, D., Mozharov, A., Sharov, V., Kolchanov, D., MacHnev, A., Golubev, V., Smirnov, A., Ginzburg, P., Makarov, S., Kurdyukov, D., Mukhin, I., 2024. Second harmonic generation and broad-band photoluminescence in

mesoporous Si/SiO2 nanoparticles. Nanophotonics 13, 3299–3309. https://doi.org/10.1515/nanoph-2024-0218.
Nora, G.I., Venkatasubramanian, R., Strindberg, S., Siqueira-Jørgensen, S.D., Pagano, L., Romanski, F.S., Swarnakar, N.K., Rades, T., Müllertz, A., 2022. Combining lipid based drug delivery and amorphous solid dispersions for improved oral drug absorption of a poorly water-soluble drug. Journal of Controlled Release 349, 206–212. https://doi.org/10.1016/j.jconrel.2022.06.057.
Purohit, H.S., Ormes, J.D., Saboo, S., Su, Y., Lamm, M.S., Mann, A.K.P., Taylor, L.S., 2017. Insights into Nano- and Micron-Scale Phase Separation in Amorphous Solid Dispersions Using Fluorescence-Based Techniques in Combination with Solid State Nuclear Magnetic Resonance Spectroscopy. Pharm. Res. 34, 1364–1377. https://doi.org/10.1007/s11095-017-2145-z.
Raina, S.A., Alonzo, D.E., Zhang, G.G.Z., Gao, Y., Taylor, L.S., 2015. Using Environment-Sensitive Fluorescent Probes to Characterize Liquid-Liquid Phase Separation in Supersaturated Solutions of Poorly Water Soluble Compounds. Pharm. Res. 32, 3660–3673. https://doi.org/10.1007/s11095-015-1725-z.
Roke, S., Gonella, G., 2012. Nonlinear light scattering and spectroscopy of particles and droplets in liquids. Annu. Rev. Phys. Chem. 63, 353–378. https://doi.org/10.1146/annurev-physchem-032511-143748.
Saal, C., Petereit, A.C., 2012. Optimizing solubility: Kinetic versus thermodynamic solubility temptations and risks. European Journal of Pharmaceutical Sciences 47, 589–595. https://doi.org/10.1016/j.ejps.2012.07.019.
Shultz, M.D., 2019. Two Decades under the Influence of the Rule of Five and the Changing Properties of Approved Oral Drugs. J. Med. Chem. https://doi.org/10.1021/acs.jmedchem.8b00686.
Stender, E.G.P., Ray, S., Norrild, R.K., Larsen, J.A., Petersen, D., Farzadfard, A., Galvagnion, C., Jensen, H., Buell, A.K., 2021. Capillary flow experiments for thermodynamic and kinetic characterization of protein liquid-liquid phase separation. Nat. Commun. 12. https://doi.org/10.1038/s41467-021-27433-y.
Sugano, K., Kato, T., Suzuki, K., Keiko, K., Sujaku, T., Mano, T., 2006. High throughput solubility measurement with automated polarized light microscopy analysis. J. Pharm. Sci. 95, 2115–2122. https://doi.org/10.1002/jps.20628.
Tarun, O.B., Dupertuis, N., Wilkins, D.M., Roke, S., 2025. Solvent Redistribution Method To Determine Solubility and Aggregation: High Throughput, Accuracy, and Sustainability. J. Phys. Chem. B 129, 8798–8805. https://doi.org/10.1021/acs.jpcb.5c03073.
Taylor, L.S., Zhang, G.G.Z., 2016. Physical chemistry of supersaturated solutions and implications for oral absorption. Adv. Drug Deliv. Rev. https://doi.org/10.1016/j.addr.2016.03.006.
Tilmann, B., Huq, T., Possmayer, T., Dranczewski, J., Nickel, B., Zhang, H., Krivitsky, L., Kuznetsov, A.I., de, S., Menezes, L., Vezzoli, S., Sapienza, R., Maier, S.A., 2023. Comparison of Harmonic Generation from Crystalline and Amorphous Gallium Phosphide Nanofilms. Adv. Opt. Mater. 11. https://doi.org/10.1002/adom.202300269.
Trasi, N.S., Taylor, L.S., 2015. Thermodynamics of Highly Supersaturated Aqueous Solutions of Poorly Water-Soluble Drugs - Impact of a Second Drug on the Solution Phase Behavior and Implications for Combination Products. J. Pharm. Sci. 104, 2583–2593. https://doi.org/10.1002/jps.24528.
Tres, F., Hall, S.D., Mohutsky, M.A., Taylor, L.S., 2018a. Monitoring the Phase Behavior of Supersaturated Solutions of Poorly Water-Soluble Drugs Using Fluorescence Techniques. J. Pharm. Sci. 107, 94–102. https://doi.org/10.1016/j.xphs.2017.10.002.
Tres, F., Posada, M.M., Hall, S.D., Mohutsky, M.A., Taylor, L.S., 2018b. Mechanistic understanding of the phase behavior of supersaturated solutions of poorly water-soluble drugs. Int. J. Pharm. 543, 29–37. https://doi.org/10.1016/j.ijpharm.2018.03.038.
Ueda, K., Porter, C.J.H., Goodwin, A., Taylor, L.S., 2026. The expanding role of formulations to enable oral delivery of poorly water-soluble drugs. Nat. Rev. Drug Discov. https://doi.org/10.1038/s41573-026-01407-5.
Wang, J., Matayoshi, E., 2012. Solubility at the molecular level: Development of a critical aggregation concentration (CAC) assay for estimating compound monomer solubility. Pharm. Res. 29, 1745–1754. https://doi.org/10.1007/s11095-012-0730-8.
Williams, H.D., Trevaskis, N.L., Charman, S.A., Shanker, R.M., Charman, W.N., Pouton, C.W., Porter, C.J.H., 2013. Strategies to address low drug solubility in discovery and development. Pharmacol Rev 65, 315–499. https://doi.org/10.1124/pr.112.005660.
Wyttenbach, N., Kirchmeyer, W., Alsenz, J., Kuentz, M., 2016. Theoretical Considerations of the Prigogine-Defay Ratio with Regard to the Glass-Forming Ability of Drugs from Undercooled Melts. Mol. Pharm. 13, 241–250. https://doi.org/10.1021/acs.molpharmaceut.5b00688.
Wyttenbach, N., Kuentz, M., 2017. Glass-forming ability of compounds in marketed amorphous drug products. European Journal of Pharmaceutics and Biopharmaceutics 112, 204–208. https://doi.org/10.1016/j.ejpb.2016.11.031.
Zahn, D., 2015. Thermodynamics and Kinetics of Prenucleation Clusters, Classical and Non-Classical Nucleation. ChemPhysChem 16, 2069–2075. https://doi.org/10.1002/cphc.201500231.
Zhou, L., Yang, L., Tilton, S., Wang, J., 2007. Development of a high throughput equilibrium solubility assay using miniaturized shake-flask method in early drug discovery. J. Pharm. Sci. 96, 3052–3071. https://doi.org/10.1002/jps.20913.